Additive Manufacturing xxx (xxxx) 103688

Contents lists available at ScienceDirect

Additive Manufacturing

journal homepage: www.elsevier.com/locate/addma

Influence of fluorescent dopants on the vat photopolymerization of acrylate-based plastic scintillators for application in neutron/gamma pulse shape discrimination

Caleb Chandler [a], Dominique H. Porcincula [b], Michael J. Ford [b], Thomas J. Kolibaba [c], Benjamin Fein-Ashley [a], Jason Brodsky [b], Jason P. Killgore [c, *], Alan Sellinger [a, *]

[a] Colorado School of Mines, Department of Chemistry, 1500 Illinois St., Golden, CO 80401, United States of America
[b] Lawrence Livermore National Laboratory, 7000 East Ave., Livermore, CA 94550, United States of America
[c] Applied Chemicals and Materials Division, National Institute of Standards and Technology, Boulder, CO 80305, United States of America

ARTICLE INFO

Keywords:
Vat photo-polymerization
Plastic scintillator
Digital light processing
Fluorophore
Radiation detection

ABSTRACT

Plastic scintillators, a class of solid-state materials used for radiation detection, were additively manufactured with vat photopolymerization. The photopolymer resins consisted of a primary dopant and a secondary dopant dissolved in a bisphenol A ethoxylate diacrylate-based matrix. The absorptive dopants significantly influence important print parameters, for example, secondary dopants decrease the light penetration depth by a factor $> 12\times$. The primary dopant 2,5-diphenyloxazole had minimal impact on the printing process even when loaded at 25 % by mass of the resin. Working curve measurements, which relate energy dose to cure depth, were performed as a function of feature size to further assess the influence of dopants. Photopatterns smaller than 150 μm width had apparent increases in critical energy dose compared to larger photopatterns, while all resins maintained printed features in line gratings with 50 μm of separation. Printed scintillator monoliths were compared to scintillators cast by traditional molding, demonstrating that the layer-by-layer printing process does not decrease scintillation response. A maximum light output of 31 % of a benchmark plastic scintillator (EJ-200) and successful pulse shape discrimination were achieved with 20 % by mass 2,5-diphenyloxazole as the primary dopant and 0.1 % by mass 9,9-dimethyl-2,7-distyrylfluorene as the secondary dopant in printed scintillator samples.

1. Introduction

A scintillator is a material used for radiation detection that produces light when interacting with ionizing radiation [1–4]. One type of scintillator material is plastic scintillators. Plastic scintillators are generally prepared using an aromatic polymer matrix, such as polystyrene, and have small molecule fluorescent dopants dissolved in the solid. To enable certain modes of advanced detection, a primary dopant is often added in large amounts (> 20 % by mass) to facilitate energy transfer of excited states from the matrix [2,8]. A small amount (< 1 % by mass) of secondary dopant, sometimes called a wavelength shifter, is added to the plastic to prevent concentration quenching effects and produce pulses of scintillation light [3]. A photomultiplier tube, photodiode, or CCD camera are often employed to count scintillation pulses or to engage in imaging. Plastic scintillators produced by additive manufacturing (AM) have recently been reported, allowing for fabricating novel radiation detector geometries [5–7].

The desired geometry of scintillator solids can vary significantly based on their final application, ranging from pixels of a desired aspect ratio, large slabs, or complex assemblies consisting of discrete regions with dissimilar scintillation properties. In some cases, additive manufacturing of complex scintillators enables advanced detection capabilities, such as directional detection, that would not be possible or easily achieved through traditional casting and machining of scintillators [5].

Abbreviations: AM, additive manufacturing; BPA-EO2-DA, bisphenol A ethoxylate diacrylate; 9,10-DPA, 9,10-diphenylanthracene; DLP, digital light processing; D_p, penetration depth; E_c, critical energy dose; LO, light output; LSCM, laser scanning confocal microscope; POPOP, 1,4-bis(5-phenyl-2-oxazolyl) benzene; PPO, 2,5-diphenyloxazole; PSD, pulse shape discrimination; FoM, figure of merit; SFS, 9,9-dimethyl-2,7-distyrylfluorene; TPO-L, ethyl phenyl-(2,4,6-trimethylbenzoyl) phosphinate; VP, vat photopolymerization

* Corresponding authors.
E-mail addresses: jason.killgore@nist.gov (J.P. Killgore), aselli@mines.edu (A. Sellinger).

https://doi.org/10.1016/j.addma.2023.103688
Received 13 February 2023; Received in revised form 12 May 2023; Accepted 1 July 2023

Traditionally cast scintillator plastics have required a degree of hardness that allows mechanical machining and polishing in subsequent processing steps, but AM scintillators can remove this requirement by directly printing a detector-ready material.

In order for a material to be considered viable as a scintillator, the scintillation response is evaluated in several ways. Light output (LO) and pulse shape discrimination (PSD) are two important metrics for plastic scintillators, where LO is defined as the number of photons produced in response to a known dose of incident ionizing radiation [4]. LO is commonly measured as a response relative to a commercially available plastic scintillator such as Eljen's EJ-200 product,[1] which has a light output reported at 64 % of anthracene single crystal. PSD is a property that only some specific plastic scintillators possess. Plastics doped with large amounts of primary dopant can produce pulses of scintillation with distinct decay times depending on the identity of the incident ionizing radiation. Massless radiations (e.g., gamma rays) produce shorter decay times while alpha particles or neutrons produce light with longer decay times. 3D printed plastics have been reported with PSD capabilities [9]. The discrimination capability is expressed as a figure of merit (FoM) that describes the difference in the pulse shapes [10]. An FoM of 1.27 can be considered a lower threshold for efficient discrimination and is derived from 3σ separation of two gaussian distributions [11].

For state of the art plastics that contain an aromatic polymer matrix, PSD FoM of just over 3 has been reported [8]. When using non-aromatic matrices, the FoM decreases; for example, plastic scintillators that used poly(methyl methacrylate) as the matrix have been reported with an FoM around 2 [12]. This decrease in FoM for non-aromatic matrices is particularly relevant for vat photopolymerization as many resins rely on non-aromatic monomers for fast printing. Non-aromatic monomers that are multifunctional with moieties common to the printing process (e.g., acrylates, epoxides, thiol-enes) can be easily procured, but do not always lend themselves towards efficient scintillation. The reliance of vat photopolymerization on non-aromatic monomers suggests that there is a balance between printability and performance of scintillators made using this process.

Plastic scintillator AM literature thus far has focused on vat photopolymerization (VP) of precursor resins using a digital light processing (DLP) or stereolithography (SLA) printer setup, in addition to some work on thermoplastic extrusion [6,7,13–15]. Styrenic monomers are difficult to print through photo-initiated methods due to their relatively slow rates of radical polymerization, so printing has been made possible only by adding copious amounts of crosslinker which can lower scintillation light output. Other efforts to develop photocationic polymerization of styrenic monomers toward AM printing have also been reported [16]. Alternatively, other reports described the use of matrices that are more common in VP, like those with acrylate or methacrylate functionality [6,12,15,17,18]. Recent work from Frandsen et al. has shown photocuring of scintillator formulations with good detection performance using isobornyl acrylate-based resins [19]. The bisphenol A chemical motif has been implemented as a crosslinker in previous studies of photopolymerized scintillators, and in recent reports on printing of reactive fluorescent crosslinkers in a bisphenol A acrylate matrix [15,20,21]. Overall, these reports show that acrylate and/or methacrylate functionalized bisphenol A materials can achieve promising detector capabilities in printed components, and any work focusing on vat photopolymerization would benefit further from an in-depth analysis of the printing process itself. Parameters such as light penetration depth and critical energy dose can be used to compare necessary print conditions, and study of photocured solids through microscopy can reveal inconsistencies in the print process at small length scales. In this work, a reactive bisphenol A diacrylate is used as a scintillator matrix material and the printing process is characterized as well as the scintillation performance. A deeper understanding of the printing process highlights the critical relationship between the fluorescent dopants necessary for scintillation and their impact on the photopolymerization process.

One subset within AM and VP is DLP, which is a process by which a solid part is formed from a vat of material when a digitally-masked light source initiates solidification against the surface of a mobile build plate (Fig. S1) [22–24]. The upward motion of the build plate through the vat exposes new layers of unreacted resin to form the desired geometry in a layer-by-layer fashion. A variety of functional materials have been prepared via vat photopolymerization approaches, including soft materials for tissue constructs and dental applications, and other functions such as microfluidics and electrical conductors [22,25,26]. The resolution of the print system is determined by an optical assembly rather than a nozzle shape, which allows for the printing of much finer structures when compared to extrusion-based methods. Some DLP systems have resolution below 10 μm, while extrusion-based methods are limited in x, y, and z dimensions to several hundred microns, typically [27]. DLP printing is an excellent method for producing the high resolution and transparent scintillator parts of interest, including pixelated arrays, checkerboards, or other complex geometries.

To additively manufacture plastic scintillators by DLP, the influence of dopants on the printing process must be understood. Fluorescent dopants common to plastic scintillators are carefully selected so that their absorbance and fluorescence allow energy transfer and emission that is within the optical range of the detector (e.g., secondary dopant emission around 420 nm). However, strong absorbances of the dopants around 290 nm and 365 nm may overlap with light sources in the near-UV that are useful for printing. Furthermore, in the development of PSD capable plastics, larger concentrations (> 20 % by mass) of strongly absorbing small molecules are added than would be normal for a standard DLP resin. Thus, these small molecules will directly affect the penetration of light into the resin and may secondarily affect other characteristics of the resin such as cure kinetics or viscosity, which could limit print speed, resolution, and fidelity.

This work examines the impacts of fluorescent dopants on the printing process and on scintillation performance. Working curve measurements are used to assess how dopants affect the depth of light penetration (D_p) and the critical exposure dose (E_c) of the resin. The working curve analysis is further expanded to consider the influence of feature size on D_p and E_c, providing insight into the consistency of optimal process conditions with respect to varying photomask dimensions. The LO and PSD of samples prepared through photocured casting in a mold were compared to samples printed with different dopants to evaluate the effect of printing on scintillator performance. Successful PSD was demonstrated for some formulations, and overall, we show that dopants can be incorporated into high resolution VP resins to make efficient scintillating materials with some dopants having a significant impact on the conditions necessary for printing.

2. Materials and methods

2,5-diphenyloxazole (PPO), 1,4-bis(5-phenyl-2-oxazolyl) benzene (POPOP), 9,10-diphenylanthracene (9,10-DPA), bisphenol A ethoxylate diacrylate (BPA-EO2-DA, $M_n \approx 512$ g mol^{-1}, EO per unit phenol ≈ 2, containing 1000 ppm monomethyl ether hydroquinone inhibitor), acetic acid (glacial, ReagentPlus ≥ 99 %), and 3-(trimethoxysilyl) propyl methacrylate (98 %) were purchased from Sigma Aldrich. Ethyl phenyl-(2,4,6-trimethylbenzoyl) phosphinate (TPO-L) was purchased from AmBeed. Ethanol (200 proof) was purchased from Rocky Mountain Reagents. 9,9-dimethyl-2,7-distyrylfluorene (SFS) was synthesized according to a previous publication [28]. All reagents were used as received without further purification.

[1] Certain commercial products and instrumentation are named in this work for the sake of reproducibility. Such identification does not constitute an endorsement by NIST.

Resins were formulated by weighing out initiator and dopants into a vial or jar and then adding bisphenol A ethoxylate to dissolve the solids. It was often necessary to heat the resin to 60 °C overnight and vortex vigorously to effectively dissolve and mix the components of the resin. All resins were stable to this thermal process, as shown in differential scanning calorimetry experiments (Fig. S2).

Optical characterization of liquid resins was conducted on a Thermo Fisher Nanodrop One UV–vis with a 30 μm path length, and a Beckman Coulter DU 800 UV–vis spectrometer after dilution in cyclohexane. Differential scanning calorimetry (DSC) was completed using a TA Instruments Q2000 DSC from − 20 °C to 200 °C under 40 mL min^{-1} nitrogen flow. PhotoDSC experiments were completed with an Omnicure S2000 photon source attachment and 365 nm notch filter at ≈ 2 mW cm^{-2} optical power under 40 mL min^{-1} nitrogen flow. Thermogravimetric analysis (TGA) was conducted using a TA Instruments TGA Q500. All prints were completed on a Kudo 3D Micro DLP Printer with a 365 nm lamp, and spectral characterization of all light sources used can be found in Fig. S3.

A combination of 3D (multi-layered) and 2.5D (single layered) prints were fabricated for the studies. All prints were completed using 50 μm layer steps and 25 μm nominal lateral resolution. Exposure times were varied between 1 s and 10 s at 20 mW cm^{-2}, as specified. The build plate was raised at 10 mm min^{-1} and lowered at 150 mm min^{-1}, with a 0.5 s delay after lifting. The lift height was 5 mm after the first layer, 4 mm after the three following layers, and 3 mm for the rest of the layers. 3D prints were subject to two hours of UV post cure with a 365 nm lamp at 3–4 mW cm^{-2} optical power. 2.5D prints were not UV post cured.

The 2.5D prints were used for working curve measurements and features size tests. To prepare samples, a glass cover slip (≈ 150 μm × 24 mm × 55 mm) was placed on the print plane of the Kudo 3D Micro after the vat was removed. Photocurable resin was loaded onto the slide to a height of several millimeters and held in place by surface tension (ensuring that resin depth >> cure depth). Exposure through the bottom face of the cover slip initiated photopolymerization up to some cure depth in the resin on the other side. A schematic of this procedure is included as Fig. S4. This procedure worked well with unfunctionalized cover slips; however, methacrylate functionalized cover slips were used when printing extremely delicate or thin features to enhance adhesion and preserve the solid for subsequent microscopy. The procedure used for glass functionalization can be found in the Supplementary information. For working curve measurements, 1 mm × 1 mm squares were printed at 16 increasing exposure durations, with 3 replicates per duration. For feature size tests, samples consisted of line gratings of decreasing size, all at 50 % duty cycle. The lines were 5 mm long, with widths from 25 μm to 250 μm in 25 μm steps, plus 500 μm (corresponding to pixel pitches from 1 pixel to 20 pixels) in Fig. S5.

3D prints of 25.4 mm square cubes were used for scintillator testing. Cubes were prepared from resins formulated with BPA-EO2-DA as a matrix material, 0.1 % by mass TPO-L as a photo-initiator, 20 % by mass PPO as a primary dopant, and 0.1 % by mass of either 9,10-DPA, POPOP, or SFS as a secondary dopant. Unless otherwise specified, resins will be referred to by the identity of their secondary dopant. Scintillator control samples were prepared by casting the photocurable resin in square silicone molds that were open on the top face. Curing was accomplished by irradiating the resin in the open face molds using a single 365 nm 20 mW cm^{-2} lamp.

The cure depths of working curve prints were measured using a Mitutoyo Litematic VL-50A low-force micrometer. All working curves were fit with Jacobs' basic working curve equation:

$$C_d = D_p \ln\left(\frac{E_0}{E_c}\right) \quad (1)$$

where C_d is the cure depth or height of polymerized resin, D_p is the light penetration depth (depth at which light is attenuated to $1/e$ (i.e., 37 %) of incident intensity), E_0 is the incident light intensity, and E_c is the critical energy dose (the dose at which gelation occurs). When using the Jacobs' working curve equation to linearly fit C_d as a function of ln (E_0), the D_p can be found as the slope of the line and the x-intercept provides an E_c. C_d is measured with micrometer or microscope, and E_0 is specified as a print parameter.

The full 2.5D shape of feature size test prints were measured using a Keyence VK-X1000 laser scanning confocal microscope (LSCM) with 405 nm wavelength at a 10 × objective. Open-source software (Gwyddion) was used to analyze LSCM images. After baseline correction, feature height was determined by fitting local maxima in the height distribution that represented the height difference between the top surface of the glass slide and top surface of the photopolymer solid. Widths were measured manually as an average of 5 lengths perpendicular to the 5 mm line grating.

Scintillation performance was measured by coupling samples to a Hamamatsu R6231 100 SEL photomultiplier tube with optical grease and wrapping the scintillator in Teflon tape. ^{137}Cs was used for irradiation, and the photomultiplier tube output was recorded using a 14-bit high resolution CompuScope 14200 waveform digitizer. Light output measurements were made with (25.4 × 25.4 × 25.4) mm^3 cubes of scintillator and were compared to an EJ-200 standard of the same dimensions. For PSD measurements, the scintillators were exposed to a ^{252}Cf source shielded by 5.1 cm of lead, which reduced the gamma-ray flux. The total charge of a scintillation pulse was determined by integration of the pulse over time, and the slow component of the charge was compared to the total, allowing for the calculation of FoM following previous methodology [29,30].

3. Results

3.1. Spectral absorbance

Absorbances of individual components were measured in dilute cyclohexane solutions, shown in Fig. S6a and summarized in Table 1. The photoinitiator TPO-L absorbs light most strongly at wavelengths less than 420 nm; any competing absorption in this region by the other components of the resin must be considered to understand possible effects on photocuring. From the absorbance data in Fig. S6a, dilute solutions of BPA-EO2-DA and PPO do not appear to contribute to significant attenuation of light above 295 nm and 347 nm, respectively. A closer inspection of PPO's contribution to absorbance (Fig. S6b.) shows that at concentrations of 20 wt%, a measurable tail of absorbance extends past 365 nm. Absorbance is inversely proportional to penetration depth, so the absorptive contribution from PPO is more significant to Dp in the case of the 9,10-DPA containing resin than in resins that have larger absorbance contributions from POPOP or SFS. Subtracting the absorbance of PPO from the 9,10-DPA resin theoretically increases Dp by 50 μm, while the POPOP and SFS resins would only increase less than 2 μm. The difference in magnitude in the effect of PPO is due to the inverse log relationship between absorbance and D_p, where resins with larger absorbances will see smaller impacts due to changes. Overall, it is the secondary dopant that dominates absorption at the 365 nm wavelength

Table 1
Table of absorbance cutoffs and maxima measured in cyclohexane solutions.

Components	Absorbance peak (nm)	Absorbance cutoff (nm)
BPA-EO2-DA	275, 285	295
PPO	301, 314	347
9,10-DPA	353, 371, 391	412
POPOP	341, 356, 375	397
SFS	366, 383	413
TPO-L	372	430

and regulates D_p. Additionally, the secondary dopant, which is critical for scintillation light output, absorbs light in a range that is similar to the range of a photoblocker additive, which is often used in VP to control light penetration depth (D_p) [31,32].

The absorbance of three formulations containing BPA-EO2-DA, 20 % by mass PPO, 0.1 % by mass TPO-L, and 0.1 % by mass secondary dopant, and a resin with only BPA-EO2-DA and 0.1 % by mass TPO-L were also measured without dilution, as shown in Fig. 1. At 365 nm, the resin doped with SFS absorbed more than that with POPOP, and the 9,10-DPA resin was the most transmissive. The molar concentrations of the secondary dopant vary slightly between resins with 3.48 mM for 9,10-DPA, 3.16 mM for POPOP, and 2.89 mM for SFS however, these differences do not account for differences in the absorbance, especially since the resin with SFS has the strongest absorbance but lowest concentration. For further comparison, there was 3.64 mM of the photoinitiator TPO-L in each resin. With the similar concentrations of each secondary dopant, the difference in attenuation was mostly dictated by the molar absorption coefficient. Molar absorption coefficients were calculated at 365 nm by normalizing the absorbance for concentration and path length, and the calculated coefficients agreed well with values reported in literature (Table 2). The values were also compared to the molar absorption coefficient of the Mayzo OB + photoblocker added to the open source DLP resin, PR-48, at a concentration of ≈ 4.3 mM [33,34].

3.2. Working curve analysis

A working curve measures the depth of cured resin as a function of light exposure dose (E_0), allowing selection of exposure conditions for a given programmed layer thickness while printing a 3D part. Working curve samples were prepared with 365 nm light at 2.4 mW cm^{-2} intensity with formulations containing BPA-EO2-DA, 25 % by mass PPO, 0.1 % by mass TPO-L, and 0.1 % by mass secondary dopant. Working curves were also prepared at 20 mW cm^{-2} with formulations containing BPA-EO2-DA, 20 % by mass PPO, 0.1 % by mass TPO-L, and 0.1 % by mass secondary dopant to consider resin that produced solids that were more stable against dopant precipitation (due to less primary dopant loading), and higher intensity print conditions that were much faster. All measured curves exhibit the expected log-linear dependence predicted by Beer-Lambert absorption of light.

The resulting penetration depth (D_p) and critical energy dose (E_c) were determined by least squares regression fit of the working curve for each resin and are shown in Fig. 2. D_p describes attenuation of light by the resin, derived from the working curve slope, and E_c is the dose necessary for gelation to begin, found as the x-intercept of the working curve [37,38]. As indicated by the overall working curve, changes in these values were minimal with the addition of PPO for resins that contained a secondary dopant. D_p values were within 6 μm of each other, and E_c values did not vary in a monotonic fashion with and without PPO. Notably, some data points were forfeited at lower exposures in the resins with 25 % by mass PPO because of patterns delaminating from the glass surface. The delamination is attributed to the plasticizing effect of PPO in the gelled solids, which has been observed in other scintillating plastics [39].

As summarized in Table 3, the D_p of the resins correlates with D_p values calculated from the absorbance in Fig. 1, with SFS having the highest attenuation (i.e., the smallest penetration depth), followed by POPOP, and then 9,10-DPA (Table 3). PhotoDSC results of the same resins shown in Fig. S7 feature exotherms with tails that correlate with D_p. Samples prepared for photoDSC are thicker than a single layer would be in the print process and a longer exotherm tail may be caused by absorbers limiting the depth of reaction in the sample and extending the reaction time. Working curve preparation, on the other hand, is analogous to the vat photopolymerization procedure. According to the working curves, when no secondary dopant is added to the resin, the D_p increases by two orders of magnitude to a depth of several millimeters (Fig. S8). However, solids polymerized without any 365 nm absorber were undesirable due to local irregular regions of solidification that extended several millimeters from the part in the z-axis. The formation of these irregular regions was due to the large D_p of the resin without any absorber and was not observed with scintillating resins that contained secondary dopant. Scintillator resins that contained secondary dopant were able to achieve layers of 50 μm at exposures of 24.9 mJ cm^{-2} (9,10-DPA), 34.6 mJ cm^{-2} (POPOP), and 176 mJ cm^{-2} (SFS). The Kudo Micro 3D printer used for this study was capable of intensities up to 24 mW cm^{-2} which enabled print layer times of several seconds at a chosen intensity of 20 mW cm^{-2}. Working curves were also measured at 20 mW cm^{-2} with less primary dopant (Fig. S9) with no significant changes in D_p or E_c when compared to working curves measured with 2.4 mW cm^{-2} (Table 3).

3.3. Feature size effects

After a basic understanding of resin print performance was established through spectroscopy and working curves, laser scanning confocal microscopy was used to further characterize printing. The widths and heights of the lines in the 2.5D line grating prints were measured and plotted as a function of programmed feature size and exposure conditions. Widths varied at the base and top of each line in the z-axis, and both were measured. Samples were prepared at three different doses, holding a 20 mW cm^{-2} intensity for 2 s, 4 s, or 8 s, to probe how print parameters impact resolution in the different resins.

Presented in Fig. 3, the cure depth of solidified features increased with exposure time and feature width for all resins. Each resin exhibited a plateau range above ≈ 150 μm programmed feature width where the height of features (i.e., the cure depth) became constant regardless of the programmed width. When compared to the primary working curves, the heights of features within this plateau region measured using LSCM matched the traditional values. The height decreased for pro-

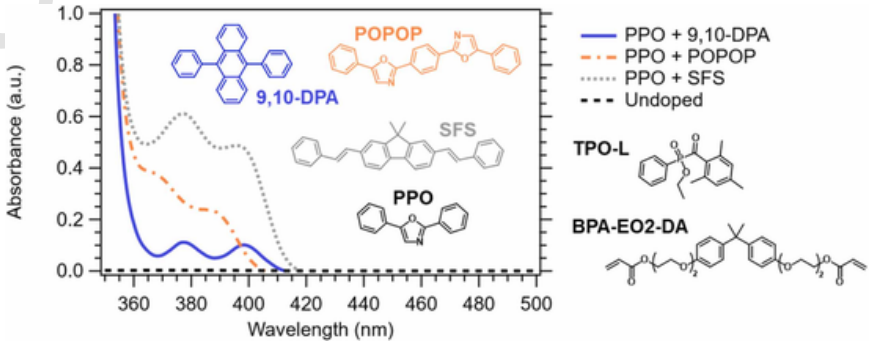

Fig. 1. Attenuation through 30 μm path length of undiluted scintillator resins consisting of BPA-EO2-DA, 20 % by mass PPO, 0.1 % by mass TPO-L, 0.1 % by mass of specified secondary. Chemical structures of resin components are also shown and labeled.

Table 2
Molar absorption coefficients at 365 nm [33,35,36].

Source	TPO-L Only	9,10-DPA	POPOP	SFS	Mayzo OB+
Resin (cm^{-1} M^{-1})	200	7000	40,700	56,700	N/A
Literature (cm^{-1} M^{-1})	150	7500	37,400	N/A	34,000

grammed widths less than 150 μm, and the magnitude of the drop was constant for each resin regardless of exposure time. Further experimentation was conducted to identify if this loss was a property of the printer's optics at small photopatterns.

Power output was measured at three conditions using a 2 cm × 2 cm square power meter. The power meter measured complete illumination over the detector area, a 50 % duty cycle of 250 μm line gratings over the detector area, and a 50 % duty cycle of 25 μm line grating over detector area. The 50 % duty cycle exposures illuminated 50 % of the detector to the photon source through the different size photopatterns. The power output of both 50 % duty cycles was halved from the total illuminated area measurement, supporting that the total power output of the printer is consistent at small feature sizes and not responsible for the height decrease. This overall consistency in printer power output does not exclude local intensity changes due to pixel overlap or other size dependent events such as diffusion, which are discussed later.

Three different doses were used for each resin in the feature width experiments, making it possible to fit sparse working curves at each programmed feature size. The D_p values from each resin as a function of feature size (Fig. 4) were consistent with those found in the micrometer-derived working curve measurements across all feature sizes. The E_c values were also consistent with the values determined from working curves measured by a micrometer for feature sizes larger than approximately 150 μm. For these experiments, E_c values began to increase for features smaller than ≈ 150 μm. At the smallest programmed width (25 μm), the E_c had increased by a value between 8 mJ cm^{-2} and 18 mJ cm^{-2}, nearly doubling for resins doped with POPOP or SFS. This increase in E_c means that initial solidification would require an increase in the necessary dose that must be considered when printing large and small features at the same time.

The resulting solids in the 2.5D line gratings were trapezoidal with bases that were wider than the tops in the z-direction. The light source was incident on the resins at the side where the wider base of the trapezoid formed. In almost all cases, the base of each line was slightly larger than the programmed width and the top was slightly smaller than the programmed width. Although the secondary dopant had large effects on height, the printed widths of the features showed no such correlation. Rather, the top widths of the trapezoidal solids were slightly shorter than the base widths across all resins, shown in Fig. 5. Width resolution was also characterized by determining the programmed feature size at which the cured solids ran together and lost separation (Table 4) (i.e., where no bare substrate is visible between the line grating). The 2 s, 4 s and 8 s exposures at 20 mW cm^{-2} intensities cause solidification at very different points on each resin's respective working curve, which can have a large impact on the timescale when features bleed together. In all cases, increasing the exposure causes features to bleed together at larger feature sizes, for a loss in resolution. The 9,10-DPA and POPOP containing resins lose separation at similar sizes for each exposure condition while the SFS containing resin maintained separation down to smaller sizes (i.e., 100 μm at 160 mJ cm^{-2}). Each resin requires a different dose of light to reach a given height, with the SFS doped resin requiring the most. Thus, at a given exposure, SFS appeared to have the best separation because it had the lowest sample height and thus the least amount of photoinitiated polymerization and associated diffusion of solidification outside the irradiated area.

3.4. 3D prints

Several complex geometries were fabricated to demonstrate that these resin formulations are functional for printing with 365 nm light in a DLP process. Exposure settings were determined from the working curve measurements of each resin and were used directly without correction or heuristic change. For example, 50 μm cure depths were targeted to print 50 μm layers using 1.25 s, 1.73 s, and 8.82 s at 20 mW cm^{-2} intensities for the 9,10-DPA, POPOP, and SFS containing resins, respectively. These conditions were used to print the logos of the collaborating author's institutions, the classic benchmark boat "Benchy", and a gyroid structure (Fig. 6). The first 250 μm (5 layers) of the print used exaggerated exposure times (15–30 × the working curve derived values) to establish a solid acrylate layer over the desired print area on the glass build plate. In the 2.5D studies, adhering acrylate solids on the glass window became increasingly difficult as feature size decreased, but this difficulty was not observed when printing small features onto a previous layer of solidified resin. Solid base layers (i.e., "burn layers") coating the glass surface were necessary for printing the gyroid geometry.

Formulated resins were stable against premature curing when stored at room temperature in the dark. They exhibited no measurable changes in curing characteristics during printing or working curve measurement after storage for 7 weeks. Thermal stability of the resins was measured through DSC experiments and also ensured that the procedure of mixing of resins at 60 °C was not initiating and propagating polymerization. Resins showed no exotherm associated with polymerization when heated from 25 °C to 150 °C (Fig. S2).

Thermal properties of solidified materials were also studied. DSC cycles from − 20 °C to 150 °C were conducted on solidified plastic made from the resins, but no glass transition or residual curing exotherms were observed (Fig. S10). TGA of the solid plastic showed stability up to

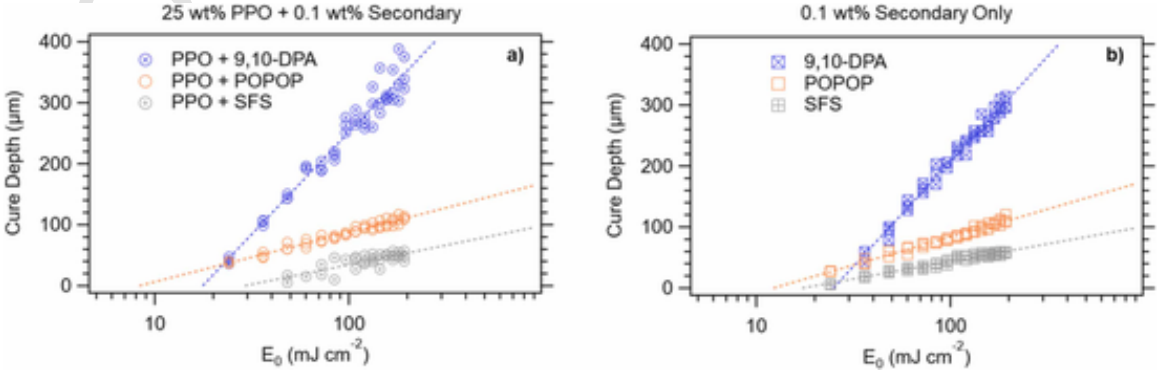

Fig. 2. Working curves for various formulations containing either 25 % by mass PPO (a) or 0 % PPO (b), with 0.1 % by mass of specified secondary dopant. Samples were prepared with 365 nm source at 2.4 mW cm^{-2}.

Table 3
D_p and E_c values calculated from working curves (WC) prepared at 2.4 mW cm^{-2} and 20 mW cm^{-2} 365 nm light, compared with D_p values calculated from UV–vis optical absorbance measurements at 365 nm.

Method		D_p (μm)			E_c (mJ cm^{-2})	
		WC @ 2.4 mW cm^{-2}	WC @ 20 mW cm^{-2}	UV–vis Abs	WC @ 2.4 mW cm^{-2}	WC @ 20 mW cm^{-2}
9,10-DPA	**PPO**	150 ± 10	143 ± 5	172 (± 2 % S.D.)	18 ± 6	21 ± 4
	No PPO	149 ± 7	–	–	25 ± 6	–
POPOP	**PPO**	35 ± 2	43 ± 2	33 (± 2 % S.D.)	8 ± 3	10 ± 3
	No PPO	40 ± 2	–	–	12 ± 3	–
SFS	**PPO**	31 ± 2	28 ± 2	26 (± 2 % S.D.)	37 ± 10	22 ± 9
	No PPO	25 ± 2	–	–	17 ± 7	–

150 °C, where mass loss corresponding to the evaporation of PPO from the plastic began to occur (Fig. S11).

3.5. Scintillator performance

Plastic scintillators are detector materials and traditional characterization of their scintillation ability includes scintillation light output, fluorescence spectroscopy, and PSD evaluation in the case of materials with large concentrations of primary dopant. The fluorescence spectra of cast and print samples was the same, centered around 420 nm (Fig. S12). Photograph of (25.4 × 25.4 × 25.4) mm^3 cubes of scintillating materials are shown in Fig. 7 alongside fabrication times, light outputs, and PSD FoMs, in Table 5. Samples were generally transparent with a slight yellow tint, and the cast and printed samples had similar light output and PSD FoM. The coupling of printed scintillators to a PMT and measurement ^{137}Cs response demonstrates the additive manufacturing of a functional scintillating detector material. The light output was ≈ 30 % of an EJ-200 commercial standard of equivalent dimensions and PSD FoMs were around the benchmark of 1.27 FoM. The scintillators doped with 9,10-DPA have FoMs below 1.20, while the FoMs for POPOP and SFS doped samples were above 1.3 with the exception of the printed POPOP doped sample. The light output was significantly lower than the EJ-200 standard; however, one major difference is that these acrylate-based scintillators contain lower aromatic content that would facilitate energy transfer. Non-aromatic poly(methyl methacrylate) plastic scintillators have shown similar light output, but higher FoM when PPO concentration was increased to 30 % by mass. It should be noted that the primary dopant, PPO, was soluble in the unpolymerized resin in amounts of up to 30% by mass but experienced precipitation within several hours once polymerization occurred. Therefore, PPO was limited at 20 % by mass to improve stability against precipitation for the printed scintillators. An increase in dopant concentration would be expected to improve PSD performance and possibly light output. Samples with 20 % by mass loading of PPO experienced surface precipitation of PPO after several weeks.

4. Discussion

Many different fluorophores have been chosen to fabricate crystalline and amorphous organic scintillators. The primary dopants in this

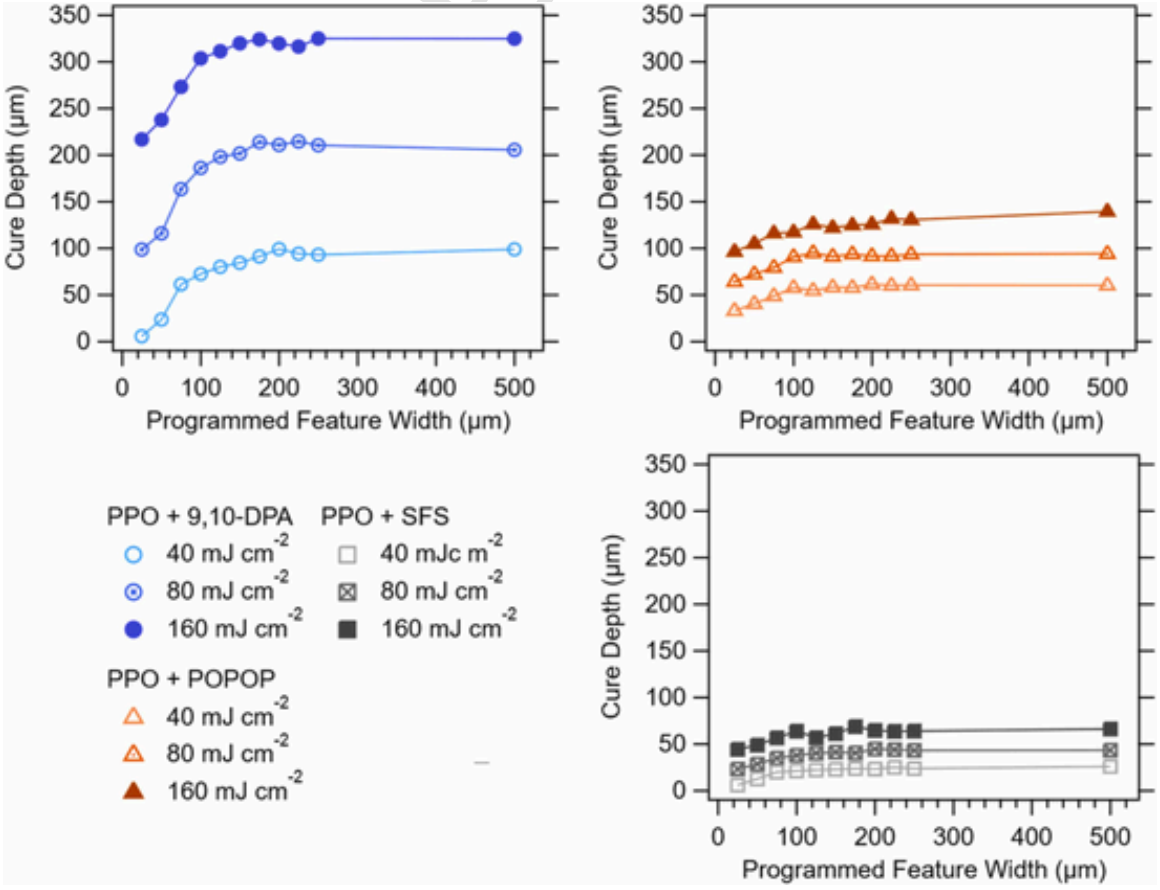

Fig. 3. Feature height as a function of size for the 3 resins containing BPA-EO2-DA, 0.1 % by mass TPO-L, 20 % by mass PPO, and 0.1 % by mass of the specified secondary dopant. Samples were prepared with 365 nm printer source at 20 mW cm^{-2}.

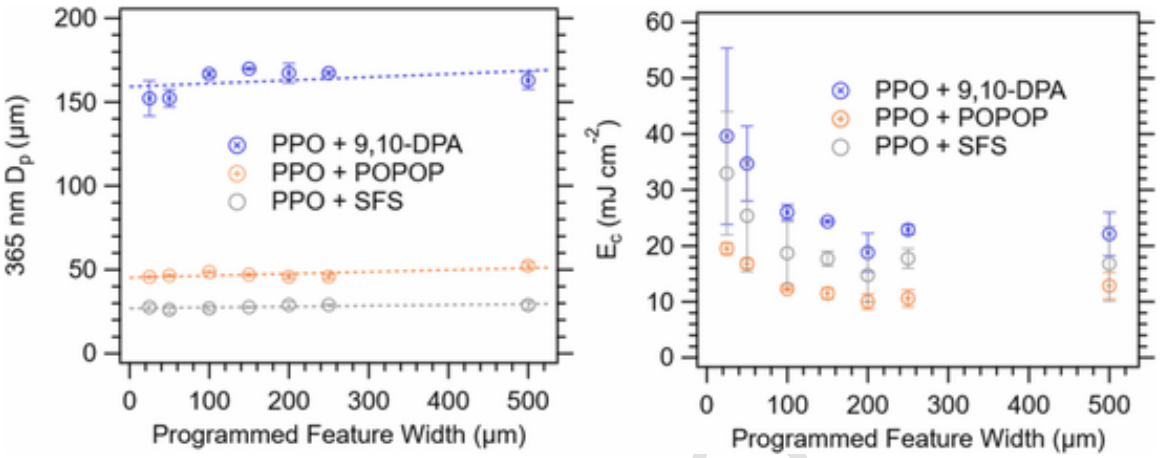

Fig. 4. Size dependent apparent D_p and E_c values from confocal microscopy working curve measurements of line gratings. Samples were prepared with 365 nm source at 20 mW cm^{-2}.

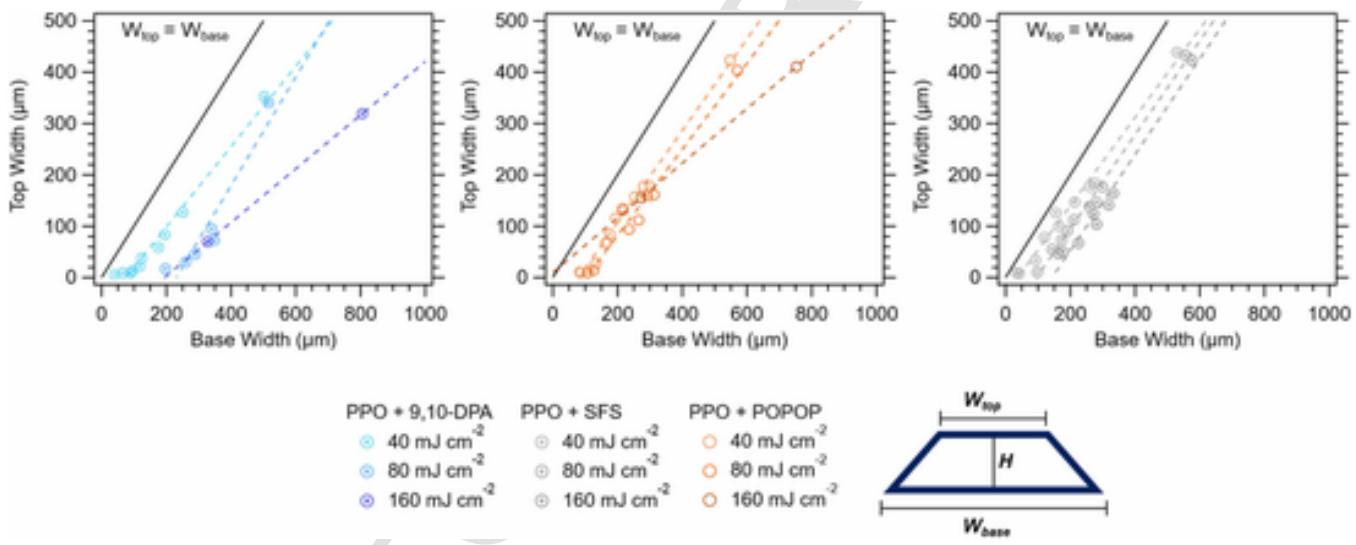

Fig. 5. Relationship between feature top width and bottom width. Trapezoidal cross-section represents widths measured on 2.5D line gratings. Samples were prepared with 365 nm source at 20 mW cm^{-2}.

Table 4
Programmed widths at which feature ran together for the 3 different resins as a function of exposure conditions. Samples were prepared with 365 nm source at 20 mW cm^{-2}.

Dose (mJ cm^{-2})	PPO + 9,10-DPA (μm)	PPO + POPOP (μm)	PPO + SFS (μm)
40	25	50	25
80	150	125	75
160	250	250	100

study were chosen for their solubility in the resin and advantageous optical properties. In the resins formulated here, the absorbance of the primary dopant and matrix was at lower wavelengths than the 365 nm source, while the secondary dopants had relatively strong absorbance at 365 nm for dilute solutions. It is common for photoblockers to be added into formulations so that D_p is limited at the active wavelengths. PR-48, a photoinitiated AM resin that is commonly used and open source, uses 0.16 % by mass of 2,5-bis(5-(tert-butyl)benzoxazol-2-yl) thiophene (Mayzo OB+) as a 365 nm absorber [34]. The secondary dopants used for scintillation have intriguing similarities to the photoblockers used in DLP resins, increasing their utility in these resins. Mayzo OB+ is incorporated in similar concentrations (0.16 % by mass at 430.6 g mol^{-1}) and has a molar absorption coefficient of ≈ 34,000 cm^{-1} M^{-1}, which results in a D_p that is between those achieved with POPOP and SFS in this work [33]. The traditional formulations used for plastic scintillators lend themselves well toward DLP resins, but a secondary dopant must be selected that can function as an efficient scintillator while properly moderating cure depth.

Cure depth can be derived from the slope of working curve measurements and also from absorbance measurements of the uncured resins themselves. D_p values taken from working curves at 2.4 mW cm^{-2} and 20 mW cm^{-2} agreed well with those calculated from optical absorbance through a known path length. In the case of resins that did not include secondary dopant, the D_p was between 20 × and 100 × larger than in doped samples and was not desirable for reproducible printing on small scales. While secondary dopant was necessary for controlling cure depth, working curves of resins that had 0 % and 20 % by mass PPO primary dopant had similar D_p and E_c despite a major amount of BPA-EO2-DA being replaced with non-reactive dopant. This consistency is a highly desirable feature of these BPA-EO2-DA-based resins, since plastic scintillators often require large concentrations of primary dopant to be capable of PSD. > 20 % by mass of primary dopant in the plastic promotes intramolecular energy transfer processes, such as triplet-triplet annihilation, which leads to distinct scintillation pulse shapes based on radiation identity.

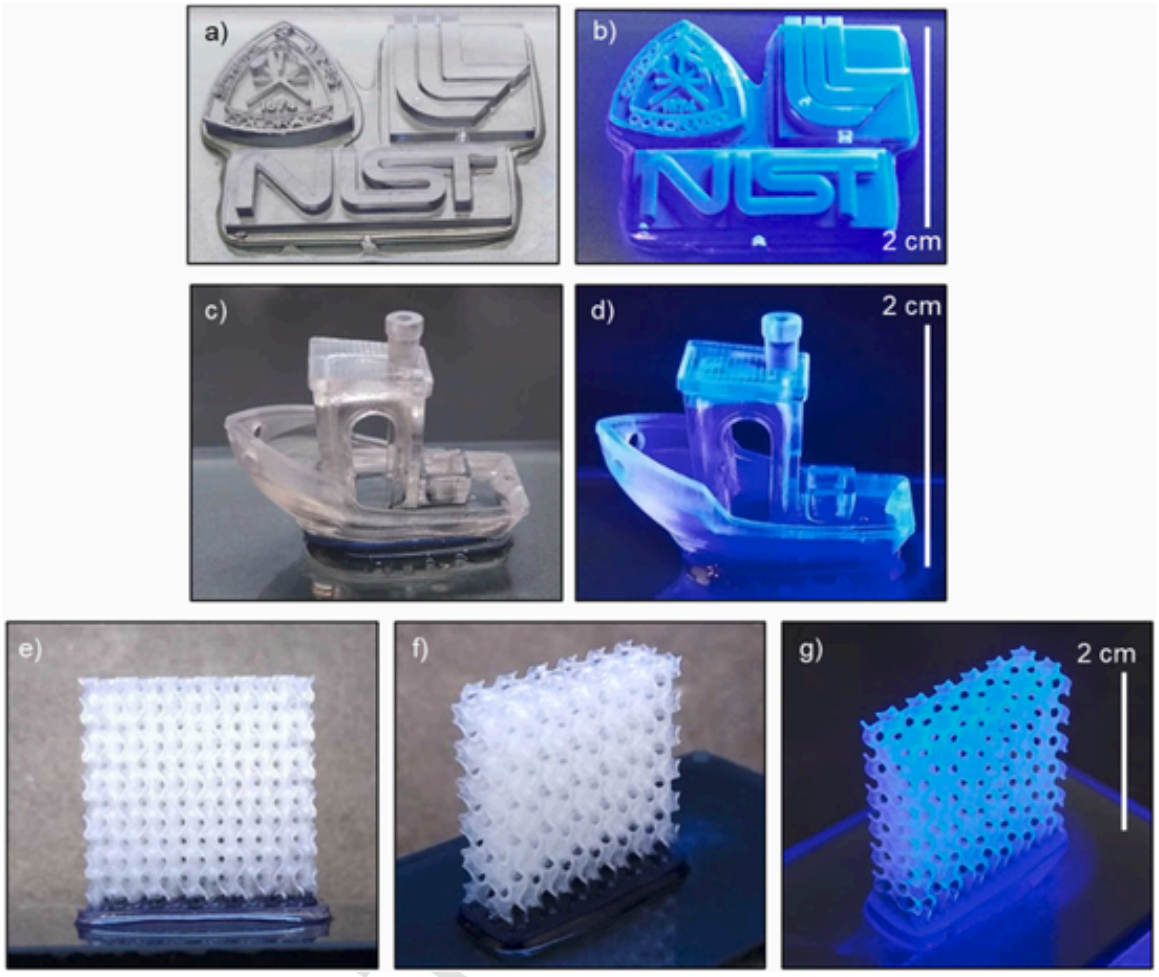

Fig. 6. Institutional logos as printed from 9,10-DPA and PPO resin, 2 cm in width (a) and under 365 nm light (b). Benchmark boat as printed using POPOP and PPO resin, 2 cm in height (c), and under 365 nm light (d). A gyroidal lattice structure as printed using SFS and PPO resin, 2 cm in height (e, f), and under 365 nm light (g). Prints were conducted with 365 nm source at 20 mW cm^{-2}.

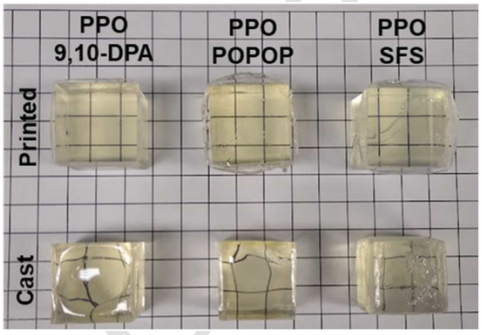

Fig. 7. Picture of cast and printed 1″ scintillator cubes. Each grid square is 1 cm on a side. Cast samples were prepared with 365 nm source at 3–4 mW cm^{-2}. Printed samples were prepared with 365 nm source at 20 mW cm^{-2}.

The primary working curves were measured using 1 mm × 1 mm square-based columns that were sufficiently large to represent printing of bulk objects and avoid any influence due to size constraints. To explore the ability of the scintillators resins to print smaller features, analogous size-dependent working curve specimens were printed and characterized with laser scanning confocal microscopy. All resins experienced a drop off in cure depth at line gratings of 5 pixels or less in width. The absolute reduction of cure depth at small feature size was a consistent value for each resin regardless of the total dose used in photopolymerization. Local changes in intensity related to pixel overlap have previously been shown to influence intensity at small feature sizes by Sun et al. and could be a factor at the small feature widths studied here [40,41]. Cross-talk between the gaussian light distributions emitted by each pixel causes a greater intensity in large pixel groups that tapers off at smaller collections of pixels. These intensity losses correlate well with the changes in cure depth reported here, however, it should be noted that Sun et al. also suggest through numerical models that intensity changes are not solely sufficient for changes in cure depth and apparent changes in E_c [40]. Other factors potential factors impacting size dependency include imperfections in the focusing or uniformity of the printer light source. In addition to illumination considerations, size effects due to oxygen inhibition in radical resins have been reported for small features with relatively larger surface area to volume ratios [42].

Table 5
Formulation, fabrication time, and scintillation performance metrics. Cast samples were prepared with 365 nm source at 3–4 mW cm^{-2}. Printed samples were prepared with 365 nm source at 20 mW cm^{-2}.

Fabrication	Fabrication time (hr:min)	LO %EJ-200	PSD FoM
Cast with 9,10-DPA	6:00	29	1.19
Print with 9,10-DPA	2:20	29	1.18
Cast with POPOP	6:00	31	1.32
Print with POPOP	2:24	25	1.15
Cast with SFS	> 12:00	36	1.31
Print with SFS	3:35	31	1.33

It is possible that diffusion-based effects such as an increased diffusion of oxygen into the region of solidification, or of radicals out of the region of solidification and into the vat, can occur at smaller print sizes [43]. Differentiating illumination considerations from transport considerations may be considered in future work.

The observed changes in feature height as a function of feature size results in an apparent change in E_c, while D_p remains constant. D_p is a function of the attenuation of light by dopants and photo-initiator, so it is expected that this value remains unchanged based on the volume of solidification. The E_c is a more complex value that is sensitive to diffusion effects as well as the concentration of reactive species. A low concentration (0.1 % by mass) photo-initiator was used in the resins to minimize potential impact on scintillation, but this low concentration may contribute to the increase in E_c for smaller programmed widths. As the resins approached single pixel exposures, boundary conditions may overtake bulk conditions and unidirectional diffusion of oligomers and reactive species leads to less solidification in the irradiated area. The loss in height was roughly proportional to each resin's D_p, with the largest for the 9,10-DPA resins where a 100 μm change in cure depth was observed between 500 μm and 25 μm width features. The POPOP and SFS containing resins lost 30 μm and 20 μm of height, respectively, which is much more reasonable to overcome for printing applications. Slightly increasing exposure times or grayscaling pixel intensity could be methods that compensate for the changes in E_c and improve overall print consistency [44].

Horizontal fidelity was also measured by observing at what size the line gratings overlapped. As the lines get smaller, the distance between them decreases until a continuous solid mass is formed. Solids formed at 2 s, 4 s, and 8 s exposures showed that resolution is preserved at smaller feature sizes when less light exposure is used. Underpolymerizing samples reduces the concentration and time for diffuse radicals to move into the space between features and reach a critical concentration of reactive species necessary to solidify. Despite having very different penetration depths, the 9,10-DPA and POPOP containing resin run together at very similar feature sizes. In contrast, SFS maintained separation much better even at 8 s exposures, which agrees with reports of absorbers increasing horizontal fidelity in photocuring resins [40]. SFS has a higher E_c than the other resins, which makes it more energy intensive for the resin to form solids. The difference in E_c between resins was unexpected since the reactive portions of the resin remain constant. It is unclear if the secondary dopants play a role during photopolymerization aside from their absorbance of light. Changes in resin composition did not instigate large changes in feature width but did control cure depth. The optics of the printer and the matrix/photo-initiator combination in the resin may play a much larger role than the absorbing dopants in determining the width resolution of the resins.

Samples were cast in molds using 365 nm lamps in tandem with the DLP print process to evaluate any light output reduction that originated from AM. In extrusion-based AM processes there is an opportunity for air to become trapped between layers as the shear-thinning ink is deposited, but this is not a problem in DLP where the layer-to-layer interface is submerged in the vat as photopolymerization occurs. The most significant difference between printed and cast parts may be the surface of the part because molds will yield smooth surfaces while a periodic textured surface is solidified from the layers in the print process. The rough surface of the printed side may offer more points of nucleation for the solubilized dopant at the layer interfaces and cause dopant precipitation to occur more readily. Cast samples experienced more oxygen inhibition at the surface compared to printed scintillators but the scintillation performance was similar for both methods. The SFS doped resin stood out by requiring much higher doses of light to polymerize the entire 25.4 mm deep volume of the mold during casting (Table 5). Overall, the time required to print scintillators was much less than that used to cast scintillators of the same dimensions and printed scintillator containing POPOP or SFS secondary dopants were able to discriminate between gamma and neutron radiations (Table 5). The D_p and E_c of the SFS containing resin make it printable through DLP at 365 nm but result in a photopolymerizable resin that is a poor choice for casting bulk material in molds. Application requirements drive what formulations provide the best resin properties for a specific case. The high molar absorption coefficient of SFS can make the BPA-EO2-DA resin highly suited for printing but limits the depths at which bulk curing might be successful. 9,10-DPA reduces the photon intensity and amount of time necessary for printing but prints smaller feature sizes the least consistently. If the light output or PSD is paramount, then SFS would offer the best scintillation performance of the formulations investigated here.

These resin formulations have several components that could be varied besides the secondary dopant, with the matrix material and photo-initiator potentially having the most dramatic impact on both print properties and scintillation. As the more prevalent component of the scintillator, the matrix material is the most likely material to interact with ionizing radiation and can have significant impacts on scintillation. The best performing matrices in literature have been styrenic and completely devoid of acrylate functionality. The carbonyls on acrylate and methacrylate groups have been known to quench energy transfer leading to scintillation [17]. Printing of organic scintillators would benefit greatly by identifying efficient matrix materials that are still able to print easily. The use of other photo-initiators, such as phenylbis (2,4,6-trimethylbenzoyl)phosphine oxide rather than TPO-L, can extend resin photoreactivity out to longer wavelengths where the increasingly popular 405 nm and 385 nm printers would be viable options for photopolymerization.

Despite the publication of over a dozen papers concerning AM of plastic scintillators in the last decade, the implementation of working curve measurements to compare print parameters in scintillator vat photopolymerization has been absent until this work. A low force micrometer and access to a vat-style 3D printer is sufficient to establish working curves and extract D_p and E_c values, which are necessary when discussing the merits of a formulation for a 3D printing process. The application of laser scanning confocal microscopy can also be extremely powerful; here, it is applied for size dependent analysis of D_p and E_c and demonstrates changes in solidification at small feature sizes involving 4 pixels or less in the DLP printer. In these functional materials, the study of fluorescent dopant effects offers opportunities to better understand small volume solidification during high resolution photopolymerization, and overall tradeoffs between formulations tailored for printing or detection.

5. Conclusions

Plastic scintillators capable of pulse shape discrimination were fabricated through DLP AM. Both the detector performance and printing behavior were evaluated to understand the impact of formulation on a series of acrylate resins. In this study using a 365 nm DLP printer, the secondary dopant acted as a photoblocker and controlled the light penetration depth of the resins to printable ranges when added in small amounts (0.1 % by mass) that were also advantageous for scintillation light output. This is contrasted with the primary dopant PPO that had minimal effect on light penetration depth, which is relevant for printing, even when added at 20 % by mass. Print resolution was analyzed through laser scanning confocal microscopy, revealing that incorporation of 9,10-DPA resulted in a severe loss in cure depth when printing small features, while incorporation of SFS and POPOP gave more consistent feature fidelity. All resins had an increase in the apparent critical exposure energy at smaller print features that impacted overall cure depth. Resin doped with SFS maintained separation between features at the smallest sizes and had the highest light output but was the most time consuming to print. The parameters derived from working curve measurements were used to determine print conditions for complex structures and monolithic scintillator samples. Printed scintillators had

light output and PSD on par with cast samples, with a maximum light output of 31 % EJ-200 and max PSD of 1.33 FoM achieved using SFS as a secondary dopant in the resin. An increase in primary dopant concentration could further enhance scintillation light output and PSD capability. Future research concerning vat photopolymerization AM of scintillators should include working curve measurements so that print properties can be compared as easily as detector properties. Fundamental science surrounding AM can benefit from this applied area of research where high-resolution printing is desirable for advanced detector fabrication.

Funding

This work was performed under the auspices of the U.S. Department of Energy by Lawrence Livermore National Laboratory under Contract DE-AC52-07NA27344, LLNL-JRNL-844539. This research was made possible by the National Institute of Standards and Technology and support from the Department of Energy and National Nuclear Security Administration through the Enabling Technology and Innovation Consortium under Award no. DE-NA0003921. This research was performed while Thomas J. Kolibaba held a National Research Council Research Associateship Award at the National Institute of Standards and Technology. Certain commercial products and instrumentation are named in this work for the sake of reproducibility. Such identification does not constitute an endorsement by NIST.

Uncited reference

[45].

CRediT authorship contribution statement

Caleb Chandler : Writing – review & editing, Writing – original draft, Visualization, Methodology, Investigation, Formal analysis, Data curation, Conceptualization. **Dominique H. Porcincula :** Writing – review & editing, Supervision, Methodology, Investigation, Conceptualization. **Michael J. Ford :** Writing – review & editing, Methodology, Investigation, Formal analysis, Conceptualization. **Thomas J. Kolibaba :** Writing – review & editing, Methodology, Formal analysis, Conceptualization. **Benjamin Fein-Ashley :** Investigation. **Jason Brodsky :** Writing – review & editing, Supervision, Project administration, Methodology, Conceptualization. **Jason P. Killgore :** Writing – review & editing, Supervision, Project administration, Methodology, Investigation, Formal analysis, Data curation, Conceptualization. **Alan Sellinger :** Writing – review & editing, Supervision, Project administration, Methodology, Conceptualization.

Declaration of Competing Interest

The authors declare that they have no known competing financial interests or personal relationships that could have appeared to influence the work reported in this paper.

Acknowledgements

Analyses were performed at MIMIC, CU Boulder (RRID:SCR_019307). We thank the Colorado School of Mines Department of Chemistry.

Appendix A. Supporting information

Supplementary data associated with this article can be found in the online version at doi:10.1016/j.addma.2023.103688.

References

[1] M. Hamel, Plastic Scintillators: Chemistry and Applications, Springer Nature, 2021.
[2] G.H.V. Bertrand, M. Hamel, S. Normand, F. Sguerra, Pulse shape discrimination between (fast or thermal) neutrons and gamma rays with plastic scintillators: state of the art, Nucl. Instrum. Methods Phys. Res. Sect. A: Accel. Spectrom. Detect. Assoc. Equip. 776 (2015) 114–128, https://doi.org/10.1016/j.nima.2014.12.024.
[3] F.D. Brooks, Development of organic scintillators, Nucl. Instrum. Methods 162 (1979) 477–505, https://doi.org/10.1016/0029-554X(79)90729-8.
[4] J.B. Birks, The Theory and Practice of Scintillation Counting, Macmillan, 1964.
[5] J.P. Brodsky, N.S. Bowden, System and Method for Neutron and Gamma Radiation Detection Using Non-Homogeneous Material Scintillator, US20210103060A1, 2021.
[6] Y. Mishnayot, M. Layani, I. Cooperstein, S. Magdassi, G. Ron, Three-dimensional printing of scintillating materials, Rev. Sci. Instrum. 85 (2014) 085102, https://doi.org/10.1063/1.4891703.
[7] S. Berns, A. Boyarintsev, S. Hugon, U. Kose, D. Sgalaberna, A.D. Roeck, A. Lebedynskiy, T. Sibilieva, P. Zhmurin, A novel polystyrene-based scintillator production process involving additive manufacturing, J. Inst. 15 (2020) https://doi.org/10.1088/1748-0221/15/10/P10019 (P10019–P10019).
[8] N. Zaitseva, B.L. Rupert, I. PaweŁczak, A. Glenn, H.P. Martinez, L. Carman, M. Faust, N. Cherepy, S. Payne, Plastic scintillators with efficient neutron/gamma pulse shape discrimination, Nucl. Instrum. Methods Phys. Res. Sect. A: Accel. Spectrom. Detect. Assoc. Equip. 668 (2012) 88–93, https://doi.org/10.1016/j.nima.2011.11.071.
[9] K. Kim, D.-G. Kim, S. Lee, J. Park, J. Son, Y.K. Kim, Neutron-gamma pulse shape discrimination using 3D-printed plastic scintillator with high-concentration PPO, in: Proceedings of the 2020 IEEE Nuclear Science Symposium and Medical Imaging Conference (NSS/MIC), 2020, pp. 1–3. ⟨https://doi.org/10.1109/NSS/MIC42677.2020.9507824⟩.
[10] M. Sénoville, F. Delaunay, M. Pârlog, N.L. Achouri, N.A. Orr, Neutron-γ discrimination with organic scintillators: intrinsic pulse shape and light yield contributions, Nucl. Instrum. Methods Phys. Res. Sect. A: Accel. Spectrom. Detect. Assoc. Equip. 971 (2020) 164080, https://doi.org/10.1016/j.nima.2020.164080.
[11] N. Zaitseva, A. Glenn, L. Carman, H. Paul Martinez, R. Hatarik, H. Klapper, S. Payne, Scintillation properties of solution-grown trans-stilbene single crystals, Nucl. Instrum. Methods Phys. Res. Sect. A: Accel. Spectrom. Detect. Assoc. Equip. 789 (2015) 8–15, https://doi.org/10.1016/j.nima.2015.03.090.
[12] H. Paul Martinez, I. Pawelczak, A.M. Glenn, M. Leslie Carman, N. Zaitseva, S. Payne, Pulse shape discrimination in non-aromatic plastics, Nucl. Instrum. Methods Phys. Res. Sect. A: Accel. Spectrom. Detect. Assoc. Equip. 771 (2015) 28–31, https://doi.org/10.1016/j.nima.2014.10.023.
[13] S. Berns, E. Boillat, A. Boyarintsev, A. De Roeck, S. Dolan, A. Gendotti, B. Grynyov, S. Hugon, U. Kose, S. Kovalchuk, B. Li, A. Rubbia, T. Sibilieva, D. Sgalaberna, T. Weber, J. Wuthrich, X.Y. Zhao, Additive manufacturing of fine-granularity optically-isolated plastic scintillator elements, J. Inst. 17 (2022) P10045, https://doi.org/10.1088/1748-0221/17/10/P10045.
[14] S. Kim, Y.-H. Seoung, Fabrication and characterization of 3D printed polyvinyl toluene based plastic scintillator, J. Korean Phys. Soc. 75 (2019) 953–956, https://doi.org/10.3938/jkps.75.953.
[15] D. Kim, S. Lee, J. Park, J. Son, T.H. Kim, Y.H. Kim, K. Pak, Y.K. Kim, Performance of 3D printed plastic scintillators for gamma-ray detection, Nucl. Eng. Technol. 52 (2020) 2910–2917, https://doi.org/10.1016/j.net.2020.05.030.
[16] C. Chandler, D.H. Porcincula, M.J. Ford, C. Hook, X. Zhang, J. Brodsky, A. Sellinger, Plastic scintillators via rapid photoinitiated cationic polymerization of vinyltoluene, ACS Appl. Polym. Mater. (2022), https://doi.org/10.1021/acsapm.2c00316.
[17] V.N. Salimgareeva, S.V. Kolesov, Plastic scintillators based on polymethyl methacrylate: a review, Instrum. Exp. Tech. 48 (2005) 273–282, https://doi.org/10.1007/s10786-005-0052-8.
[18] S. Kim, Y.-H. Seoung, Proton-induced scintillation properties of a UV-cured plastic scintillator, J. Korean Phys. Soc. 73 (2018) 1123–1125, https://doi.org/10.3938/jkps.73.1123.
[19] B.G. Frandsen, M. Febbraro, T. Ruland, T.W. Stephens, P.A. Hausladen, J.J. Manfredi, J.E. Bevins, Fast-, light-cured scintillating plastic for 3D-printing applications, J. Nucl. Eng. 4 (2023) 241–257, https://doi.org/10.3390/jne4010019.
[20] A. Lim, A. Mahl, J. Latta, H.A. Yemam, U. Greife, A. Sellinger, Plastic scintillators with efficient light output and pulse shape discrimination produced via photoinitiated polymerization, J. Appl. Polym. Sci. 136 (2019) 47381, https://doi.org/10.1002/app.47381.
[21] D.G. Kim, K. Kim, S. Lee, Y.K. Kim, Enhanced characteristics of 3D-printed plastic scintillators based on bisphenol fluorene diacrylates, Radiat. Phys. Chem. 198 (2022) 110255, https://doi.org/10.1016/j.radphyschem.2022.110255.
[22] A. Al Rashid, W. Ahmed, M.Y. Khalid, M. Koç, Vat photopolymerization of polymers and polymer composites: processes and applications, Addit. Manuf. 47 (2021) 102279, https://doi.org/10.1016/j.addma.2021.102279.
[23] F. Zhang, L. Zhu, Z. Li, S. Wang, J. Shi, W. Tang, N. Li, J. Yang, The recent development of vat photopolymerization: a review, Addit. Manuf. 48 (2021) 102423, https://doi.org/10.1016/j.addma.2021.102423.
[24] M. Pagac, J. Hajnys, Q.-P. Ma, L. Jancar, J. Jansa, P. Stefek, J. Mesicek, A review of vat photopolymerization technology: materials, applications, challenges, and future trends of 3D printing, Polymers 13 (2021) 598, https://doi.org/10.3390/polym13040598.

[25] W.L. Ng, J.M. Lee, M. Zhou, Y.-W. Chen, K.-X.A. Lee, W.Y. Yeong, Y.-F. Shen, Vat polymerization-based bioprinting—process, materials, applications and regulatory challenges, Biofabrication 12 (2020) 022001, https://doi.org/10.1088/1758-5090/ab6034.
[26] K.L. Sampson, B. Deore, A. Go, M.A. Nayak, A. Orth, M. Gallerneault, P.R.L. Malenfant, C. Paquet, Multimaterial vat polymerization additive manufacturing, ACS Appl. Polym. Mater. 3 (2021) 4304–4324, https://doi.org/10.1021/acsapm.1c00262.
[27] L.-Y. Zhou, J. Fu, Y. He, A review of 3D printing technologies for soft polymer materials, Adv. Funct. Mater. 30 (2020) 2000187, https://doi.org/10.1002/adfm.202000187.
[28] H.A. Yemam, A. Mahl, J.S. Tinkham, J.T. Koubek, U. Greife, A. Sellinger, Highly soluble p-terphenyl and fluorene derivatives as efficient dopants in plastic scintillators for sensitive nuclear material detection, Chem. – A Eur. J. 23 (2017) 8921–8931, https://doi.org/10.1002/chem.201700877.
[29] C.L. Morris, J.E. Bolger, G.W. Hoffmann, C.F. Moore, L.E. Smith, H.A. Thiessen, A digital technique for neutron-gamma pulse shape discrimination, Nucl. Instrum. Methods 137 (1976) 397–398, https://doi.org/10.1016/0029-554X(76)90353-0.
[30] N.P. Zaitseva, A.M. Glenn, A.N. Mabe, M.L. Carman, C.R. Hurlbut, J.W. Inman, S.A. Payne, Recent developments in plastic scintillators with pulse shape discrimination, Nucl. Instrum. Methods Phys. Res. Sect. A: Accel. Spectrom. Detect. Assoc. Equip. 889 (2018) 97–104, https://doi.org/10.1016/j.nima.2018.01.093.
[31] E. Geisler, M. Lecompère, O. Soppera, 3D printing of optical materials by processes based on photopolymerization: materials, technologies, and recent advances, Photon. Res. PRJ 10 (2022) 1344–1360, https://doi.org/10.1364/PRJ.453338.
[32] C. Yu, J. Schimelman, P. Wang, K.L. Miller, X. Ma, S. You, J. Guan, B. Sun, W. Zhu, S. Chen, Photopolymerizable biomaterials and light-based 3D printing strategies for biomedical applications, Chem. Rev. 120 (2020) 10695–10743, https://doi.org/10.1021/acs.chemrev.9b00810.
[33] B. Gharaibeh, M. Omar, A.J. Salazar, K. Saito, Fluorescence emission sensing in coatings: method for defects detection in coated surfaces of structural elements, Prog. Org. Coat. 58 (2007) 282–289, https://doi.org/10.1016/j.porgcoat.2006.12.005.
[34] E. Skliutas, S. Kasetaite, L. Jonušauskas, J. Ostrauskaite, M. Malinauskas, Photosensitive naturally derived resins toward optical 3-D printing, OE 57 (2018) 041412, https://doi.org/10.1117/1.OE.57.4.041412.
[35] G. Xie, Z. Shuai, Y. Huang, M. Yu, Z. Zeng, J. Yang, Use of floating acylphosphine oxide-based photoinitiators to reduce surface oxygen inhibition of UV-LED photopolymerization, Prog. Org. Coat. 147 (2020) 105716, https://doi.org/10.1016/j.porgcoat.2020.105716.
[36] I.B. Berlman, Handbook of Fluorescence Spectra of Aromatic Molecules, Academic Press, 1971.
[37] P.F. Jacobs, Fundamentals of Stereolithography, in: 1992. ⟨https://doi.org/10.15781/T24M91T5H⟩.
[38] J. Bennett, Measuring UV curing parameters of commercial photopolymers used in additive manufacturing, Addit. Manuf. 18 (2017) 203–212, https://doi.org/10.1016/j.addma.2017.10.009.
[39] A. Mahl, A. Lim, J. Latta, H.A. Yemam, U. Greife, A. Sellinger, Methacrylate based cross-linkers for improved thermomechanical properties and retention of radiation detection response in plastic scintillators, Nucl. Instrum. Methods Phys. Res. Sect. A: Accel. Spectrom. Detect. Assoc. Equip. 884 (2018) 113–118, https://doi.org/10.1016/j.nima.2017.11.091.
[40] C. Sun, N. Fang, D.M. Wu, X. Zhang, Projection micro-stereolithography using digital micro-mirror dynamic mask, Sens. Actuators A: Phys. 121 (2005) 113–120, https://doi.org/10.1016/j.sna.2004.12.011.
[41] A. Reid, J.C. Jackson, J.F.C. Windmill, Voxel based method for predictive modelling of solidification and stress in digital light processing based additive manufacture, Soft Matter 17 (2021) 1881–1887, https://doi.org/10.1039/D0SM01968B.
[42] A. Camposeo, A. Arkadii, L. Romano, F. D'Elia, F. Fabbri, E. Zussman, D. Pisignano, Impact of size effects on photopolymerization and its optical monitoring in-situ, Addit. Manuf. 58 (2022) 103020, https://doi.org/10.1016/j.addma.2022.103020.
[43] T.E. Brown, V. Malavé, C.I. Higgins, A.P. Kotula, B.W. Caplins, E.J. Garboczi, J.P. Killgore, Voxel-scale conversion mapping informs intrinsic resolution in stereolithographic additive manufacturing, ACS Appl. Polym. Mater. 3 (2021) 290–298, https://doi.org/10.1021/acsapm.0c01090.
[44] S.M. Montgomery, C.M. Hamel, J. Skovran, H.J. Qi, A reaction–diffusion model for grayscale digital light processing 3D printing, Extrem. Mech. Lett. 53 (2022) 101714, https://doi.org/10.1016/j.eml.2022.101714.
[45] Gelest, Applying a Silane Coupling Agent, Gelest, n.d. ⟨https://www.gelest.com/wp-content/uploads/09Apply.pdf⟩.